PHILOSOPHICAL TRANSACTIONS A

rsta.royalsocietypublishing.org

Research

Cite this article: Vanini S, Calvini P, Checchia P, Rigoni Garola A, Klinger J, Zumerle G, Bonomi G, Donzella A, Zenoni A. 2019 Muography of different structures using muon scattering and absorption algorithms. *Phil. Trans. R. Soc. A* **377**: 20180051. http://dx.doi.org/10.1098/rsta.2018.0051

Accepted: 12 October 2018

One contribution of 21 to a Theo Murphy meeting issue 'Cosmic-ray muography'.

Subject Areas:
particle physics

Keywords:
cosmic rays, muon tomography, muon radiography, image reconstruction, maximum-likelihood expectation maximization, absorption

Author for correspondence:
S. Vanini
e-mail: sara.vanini@pd.infn.it

Muography of different structures using muon scattering and absorption algorithms

S. Vanini[1], P. Calvini[2], P. Checchia[3], A. Rigoni Garola[4], J. Klinger[3], G. Zumerle[1], G. Bonomi[5], A. Donzella[5] and A. Zenoni[5]

[1]Department of Physics and Astronomy "Galileo Galilei", University of Padova, via Marzolo 8, 35131 Padova, Italy
[2]Department of Physics, University of Genova, Via Dodecaneso 33, 16146 Genova, Italy
[3]INFN Sezione di Padova, via Marzolo 8, 35131 Padova, Italy
[4]CNR, Consorzio RFX, Corso Stati Uniti 4, 35127 Padova, Italy
[5]Department DIMI, University of Brescia, via Branze 38, 25123 Brescia, Italy

SV, 0000-0002-9099-1535; PC, 0000-0002-8312-1531

In recent decades, muon imaging has found a plethora of applications in many fields. This technique succeeds to infer the density distribution of big inaccessible structures where conventional techniques cannot be used. The requirements of different applications demand specific implementations of image reconstruction algorithms for either multiple scattering or absorption–transmission data analysis, as well as noise-suppression filters and muon momentum estimators. This paper presents successful results of image reconstruction techniques applied to simulated data of some representative applications. In addition to well-known reconstruction methods, a novel approach, the so-called μCT, is proposed for the inspection of spent nuclear fuel canisters. Results obtained based on both μCT and the maximum-likelihood expectation maximization reconstruction algorithms are presented.

This article is part of the Theo Murphy meeting issue 'Cosmic-ray muography'.

THE ROYAL SOCIETY PUBLISHING

1. Introduction

The muon tomography technique has been proposed for years as an effective tool to investigate the content of large inaccessible volumes. So far, several applications and techniques have been successfully demonstrated, thanks to the free availability of cosmic muons, their deep penetrating power and the non-destructive nature of this technique. An exhaustive review of the different muon tomography applications can be found in [1]. Only the most prominent applications are discussed in the following section.

One widely used technique employs the Multiple Coulomb Scattering properties of cosmic muons in matter. This method, Muon Scattering Tomography (MST), was proposed in 2003 [2]. A wide range of MST applications have been demonstrated, ranging from security and environmental protection to homeland security. The first application proposed was addressed to detect heavy metals in transport containers, to contrast nuclear contraband or for the detection of the so-called orphan radioactive sources [3]. Moreover, an interesting industrial application has been demonstrated in which the interior of a blast furnace has been mapped in terms of coke, burden and reduced metal [4–9].

A different approach uses cosmic muons in the same manner as X-rays in ordinary radiography; i.e. by analysing the absorbed fraction while crossing dense volumes. The absorption technique was used for the first time in the 1950s by Eric George to measure the depth of the rock layer above an underground tunnel in Australia [10]. A similar application for mapping cultural heritage sites was proposed in the 1970s by L. W. Alvarez to inspect the Chefren pyramid for hollow vaults [11], and very recently implemented with spectacular results [12]. The technique has been successfully applied to volcano inspections to characterize the inner structures and lava domes [13–17], to mining [18], to archaeology [19], including tunnel searches [20], geological surveys [21,22], nuclear waste [23–26] and reactor monitoring [27,28].

This paper presents recent results obtained with different muon tomography algorithms applied to simulated data of some representative applications among the ones just mentioned. Scattering tomography maximum-likelihood expectation maximization (MLEM) is used to demonstrate the effectiveness of the detection of shielded nuclear material hidden in scrap metal cargos. The same algorithm is used to probe the capability of this technique to map the distribution of the materials inside a very large and dense structure such as a blast furnace. Regarding the absorption tomography approach, a completely novel algorithm called μCT has been developed, and its capability to image a spent nuclear fuel canister is evaluated, with very promising results.

2. The maximum-likelihood expectation maximization technique

The MST technique is based on multiple Coulomb scattering of cosmic muons. Charged particles, such as muons, are deflected and slowed down by crossing a target volume. The deviation angle projected on a plane passing through the incoming muon direction has a distribution which is approximately Gaussian for particles of the same momentum, with zero mean and a root-mean-square (σ) which is a function of the muon momentum p, of the material thickness X and of the radiation length X_0 according to the formula [29]:

$$\sigma \approx \frac{13.6\,\mathrm{MeV}}{pc}\sqrt{\frac{X}{X_0}}, \tag{2.1}$$

where c is the speed of light and the particle momentum unit is MeV/c. Measuring the deviation angles allows one to obtain information about the radiation length (or its inverse, the Linear Scattering Density (LSD), $\lambda = 1/X_0$) of an unknown material. Given the latter variance, and assuming a Gaussian probability density function for the scattering angles $\Delta\theta_i$ of

monochromatic muons:

$$P(\Delta\theta_i \mid \sigma_i) = \frac{1}{\sigma_i\sqrt{2\pi}}\, e^{\Delta\theta_i^2/(2\sigma_i^2)}, \tag{2.2}$$

the MLEM is a powerful technique that attempts to find the parameter values, i.e. the LSD for each voxel of the inspected volume, that maximize the likelihood function, given the observations of the scattering angle and displacement of the muon collection [30,31]. The large number of variables in the likelihood requires a high number of iterations for the algorithm to converge. Moreover, the statistical distribution of the scattering variables is heavily non-Gaussian for the broad momentum spectrum and the momentum of an individual particle is in general unknown. Therefore, the average value $\langle 1/p^2 \rangle$ of the momentum distribution is usually used in the MLEM algorithm, resulting in poorly reconstructed images, unless muon momentum is measured or estimated with other techniques, as will be explained in the following sections.

3. Scrap metal inspection

Scrap metal has been reused since the early ages of metal working, as recycling metal is extremely effective from both an environmental and economical standpoint. The metal recycling industry specializes in retrieving metal from obsolete objects to be converted into raw materials in foundries. Steel companies are confronted each day by the possible presence of radioactive materials in scrap, often in the form of shielded radioactive 'orphan' sources used, for example, in manufacturing operations or in hospital equipment. The radioactive sources are usually shielded by heavy metal casks (which are typically a few litres in volume) and are therefore not detected by the usual radiation portals. There have been hundreds of incidents worldwide of radioactive material becoming incorporated into metal products, resulting in metal contamination and a very expensive clean-up of the foundry itself.

Muon tomography applied to the inspection of scrap metal cargos at the entrance of foundries therefore presents a promising solution. This application requires:

- the capability to identify high density objects of the order of 2–5 l hidden among hundreds of cubic metres of low-density scrap metal;
- fast object detection (approx. few minutes timescale), in order to have a minimal impact on the queuing schedules of the steel mill facility; and
- optimal signal identification versus false positive alarms ratio.

We have investigated the effectiveness of muon tomography for detecting heavy shielded radioactive sources in scrap metal using a full-scale simulation of a muon portal for inspection, and reconstructing the images with the MLEM algorithm. A proper image filtering technique and the particle momentum estimation based on the muon trajectory behaviour inside the detectors is applied in the analysis.

(a) Simulation

A full-scale portal of dimensions $18 \times 5 \times 6\,m^3$ has been simulated with the GEANT4 package [32]. A sketch of the portal is shown in figure 1. The detection system is composed of four muon detectors of length of approximately 15 m: two horizontal detectors located above and beneath the container, and two lateral vertical detectors. The muon detector is designed as an assembly of modules to ease the construction, installation and maintenance, called super layers and composed of eight layers of drift tubes. Two super layers, one on top of the other and with tube axes rotated by 90°, compose one complete detector. Drift tubes each have a radius of 2.5 cm. The experimental error is accurately described in the simulation. The truck support is composed by an array of low-density material as timber wood beams to minimize the multiple scattering of the muons. A truck model with a scrap metal container of dimensions $6 \times 2.6 \times 2.5\,m^3$ and iron walls 5 mm thick is located inside the portal. Scrap metal has been generated as a collection

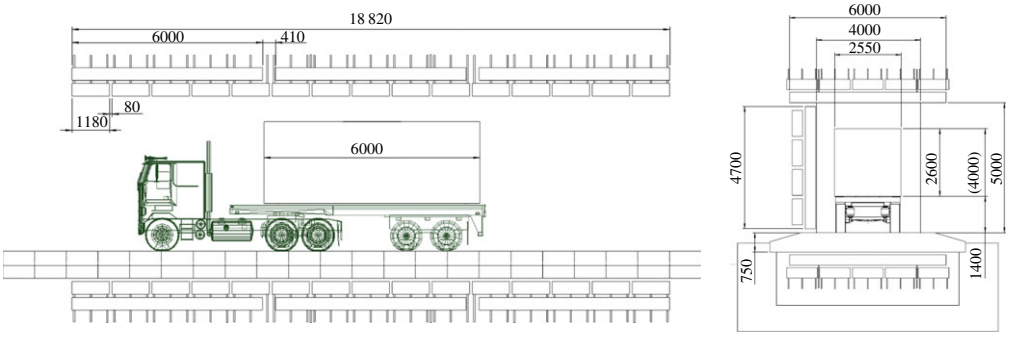

Figure 1. A sketch of the muon scanner portal, as implemented in GEANT4 simulation. (Online version in colour.)

of small iron blocks of random density between air and iron density value. The overall density average is 10% of the iron density, consistent with the measured value of fine-grained scrap metal of a real container. The radioactive source is simulated with a lead block of 2 and 5 l, roughly corresponding to the typical source shield density. The cosmic muon flux is simulated with a function fitting cosmic ray data at different zenith angles [33].

(b) Image reconstruction

The reconstruction of the three-dimensional distribution of density is performed with the MLEM algorithm. The input data of the likelihood function are the simulated incoming and outgoing muon trajectories projected on two orthogonal planes passing through the incoming direction. The scattering variables in the two planes are uncorrelated, and both the angle and the displacement are considered in the reconstruction. The tracks are computed with a straight line fit of the hits recorded in the drift tubes of muon detectors. The muon track distance from the anode wire of each tube is calculated using the signal drift time and a proper space–time relationship. The volume containing the truck to be inspected is divided into voxels (three-dimensional pixels) of homogeneous density. The edge of the cubic voxel is 5 cm and 7 cm, respectively, for the 2 l and 5 l Pb block. The algorithm performs a ray-tracing to find the voxels of the collection crossed by the most probable path of the muon, following the broken line from the incoming point, to the Point of Closest Approach (i.e. the mean point on the minimum distance segment between incoming and outgoing direction), ending at the exiting point.

Images are filtered with a $\alpha\beta$-trimmed filter [34]. This filter discards the voxels with uppermost and lowest density in a defined three-dimensional window (mask) of each voxel, and replaces the voxel density value with the Gaussian mean value computed with the remaining voxels. Figure 2 compares different kinds of filters. The α-trimmed filter is particularly effective since in this application the noise appears with impulsive components deviating from usual Gaussian distribution.

(c) Momentum estimation

A coarse determination of muon momentum is crucial for good MLEM algorithm results. Indeed, the scattering angle variance depends both on the muon momentum and the material radiation length (see equation (2.1)). For cosmic rays, the value of p^2 can vary by a factor of 10^4. Therefore, neglecting in the likelihood the exact value of the muon momentum and replacing it with the average $\langle 1/p^2 \rangle$ produces large fluctuations since low momentum muons can have large scattering angles mimicking the crossing of dense materials.

We estimate the momentum of the muon by means of the scattering in the detectors' material. As shown in figure 3, the trajectory fit residuals are larger for the low-momentum path. The strong

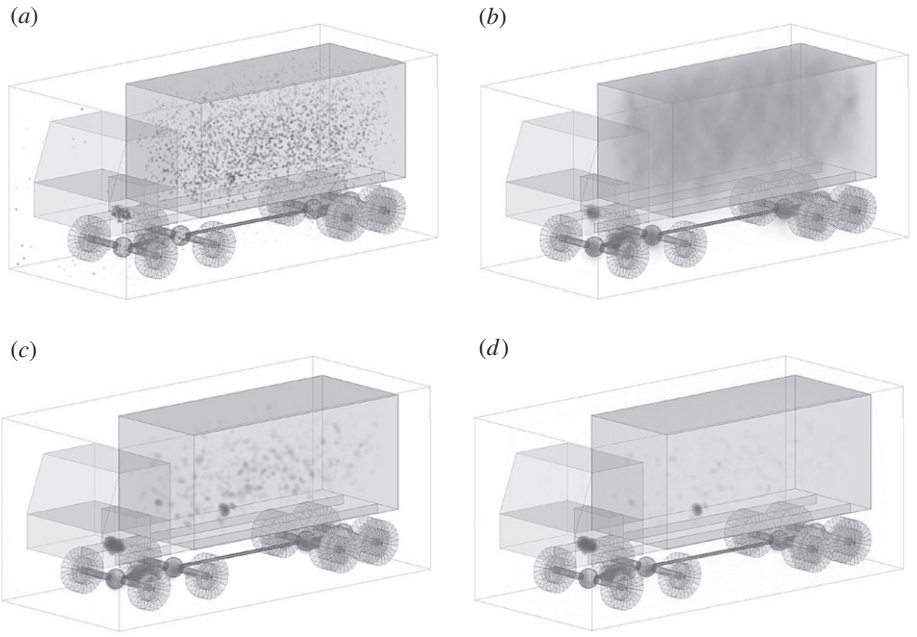

Figure 2. Comparison of different filters applied on the reconstructed image of the simulated truck filled with scrap metal and a hidden 5 l lead block. Acquisition time: 4 min. Voxel size: 5 cm. Cubic mask of 125 voxels is used in all filters. (*a*) No filter, (*b*) median, (*c*) Gaussian and (*d*) α-trim.

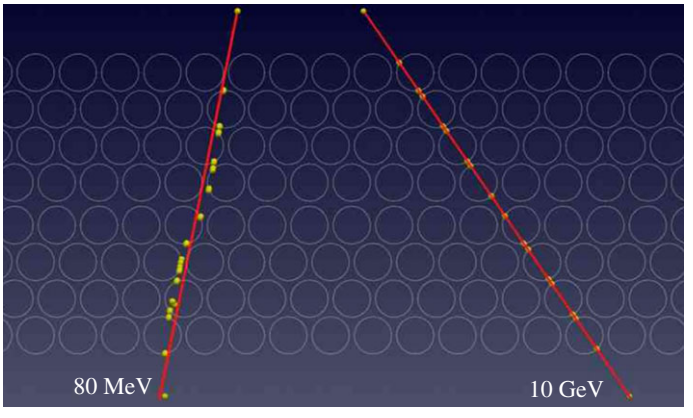

Figure 3. Simulated hits (yellow dots) for muons of low momentum (80 MeV) on the left and of high momentum (10 GeV) on the right. The fitted trajectory is displayed as a red line. Residuals from fit are larger for the low-momentum muon.

correlation of the average χ^2 of the trajectory fit with the muon momentum value available from the simulation is shown in figure 4*a*. Therefore, we divide the muon sample into five classes according to the average χ^2-value, and for each class the quantity $\langle 1/p^2 \rangle$ is computed from simulation momentum values (figure 4*b*) and used in the reconstruction likelihood.

(d) Source identification

The presence of a radioactive source candidate is confirmed if the density sum of a set of voxels is greater than a given threshold. Statistical analysis of efficiency and false alarm rate is performed.

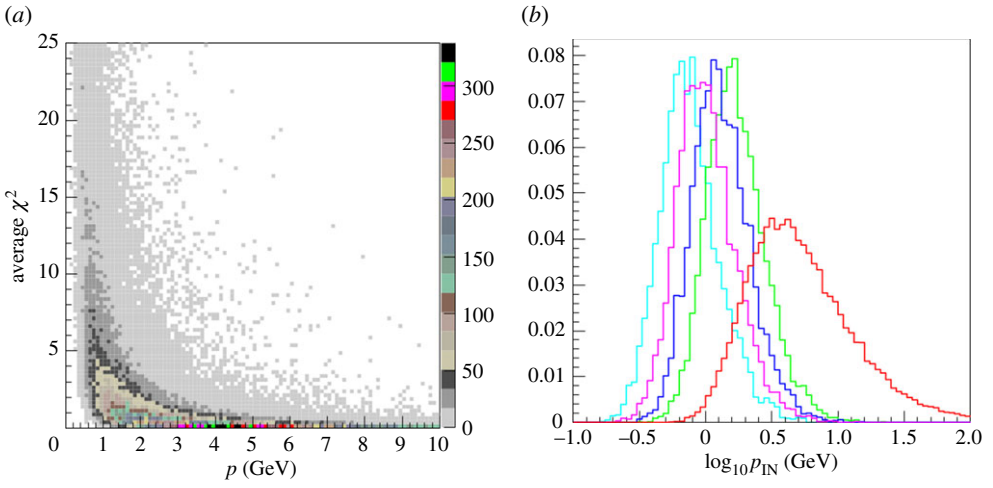

Figure 4. (*a*) Scatter plot of the average χ^2 of the muon trajectory fits versus the muon momentum value available from simulation data. (*b*) Histograms of $\log_{10} p$ for the five classes (in five different colours), according to the average χ^2.

For each source size, and for each inspection time, hundreds of independent datasets are analysed. The percentage of false alarms (FA) and the percentage of missed sources (MS) are computed as a function of the threshold value, and plotted on the same graph as the efficiency, i.e. 100%-MS (dotted line) and 100%-FA (continuous line). When a crossing between the dotted and the continuous line ordinate is less than 100%, a threshold range achieving both 100% efficiency and 0% of false alarm does not exist. Figure 5 shows the 5 l source identification graph on the top, and the 2 l graph on the bottom.

Results are summarized in table 1. The inspection times for reaching 100% efficiency and less than 1% of FA are 4 min for a 5 l shielded radioactive source, and 6 min for a 2 l source. Our results show that a portal based on muon tomography can achieve the identification of one of the smallest shielding sources present in the market in a time that meets the requirements of the steel industry.

4. Blast furnace imaging

The cosmic muons tomography techniques we developed for scrap metal cargo inspection have made great advances by means of the study of a larger and denser system: the blast furnace (BF) [4].

The objective of this project is to assess the capability of MST to produce three-dimensional images of the distribution of material density present in the blast furnace burden during operation processes. The collected information could be used for process optimization; for example, reducing the coke consumption. At present, no other available technique is known to be suitable for this purpose. The industrial requirements concerning a BF inspection are the following:

— to design a detector capable of determining the layer structure of the burden materials distribution, the properties of the cohesive zone-like shape, position and thickness, the hearth condition as the dead man situation and the level of slag/metallic melts;
— to resolve different materials as ferrous and coke, despite their modest density change; and
— to be able to handle the phenomena changing over time, i.e. the furnace internal material drop from the top to the bottom, which is of the order of approximately 8 h.

A full-scale Monte Carlo simulation is implemented for this purpose with the GEANT4 toolkit. The simulation is capable of tracking the cosmic muon trajectories through the BF and to collect

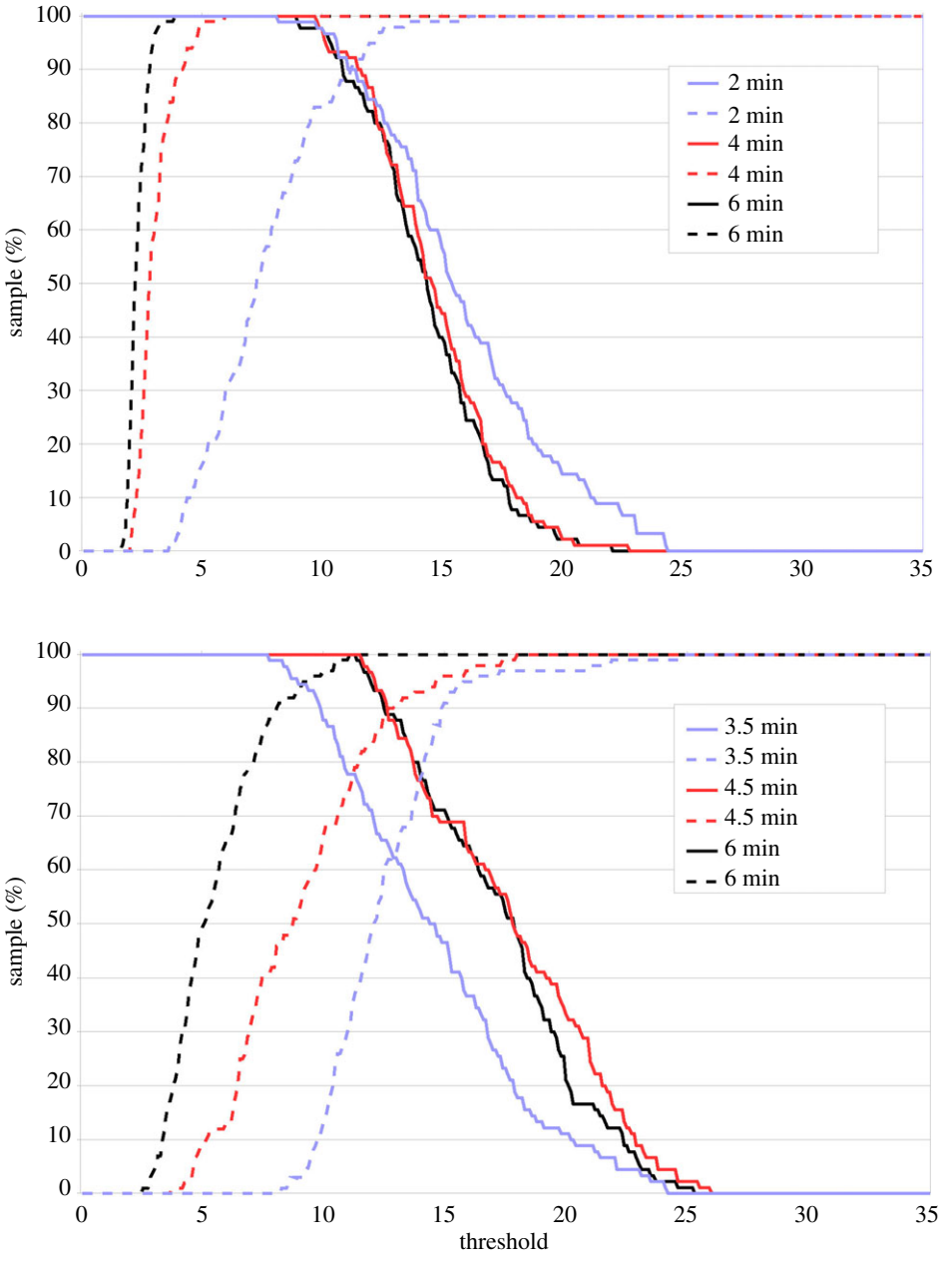

Figure 5. True-positive–negative graph: the plots of 100%-MS (dotted line) and 100%-FA (continuous line) are superimposed. The 5 l source identification graph is shown on the top of the figure, the 2 l graph on the bottom. Three exposure times are shown in each graph.

and produce all relevant information regarding particle hits on muon detectors. The simulation includes:

— a generator of muons from cosmic rays with the correct particle, angular and momentum distribution of the muon shower on the Earth surface;
— a complete description of the geometry and material composition of the structure of a typical 40 m tall blast furnace;

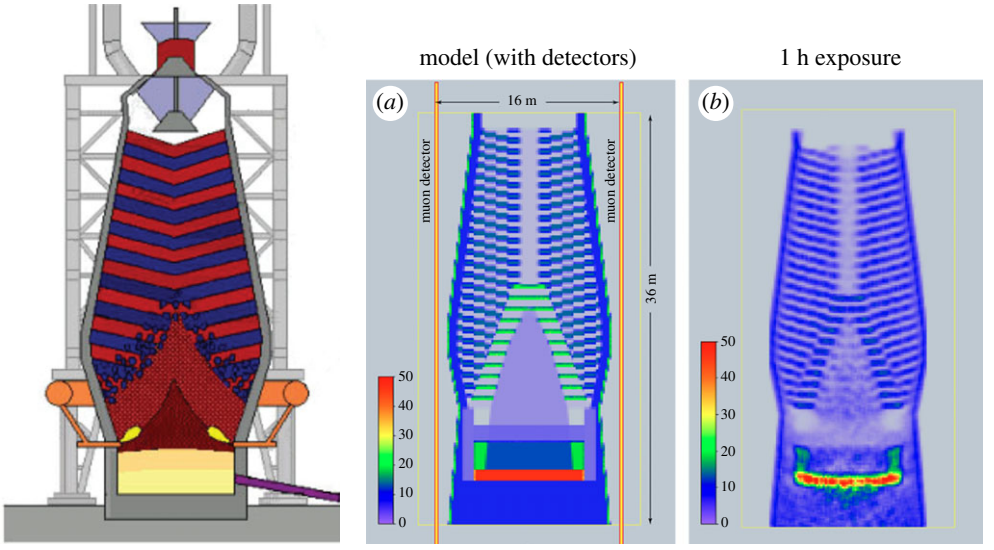

Figure 6. On the left: schematic drawing of a typical BF. The different internal volumes are distinguished by different colours. In the centre and on the right: images of the BF model: (*a*) model image of the linear scattering density as computed from GEANT4 simulation information regarding BF materials; (*b*) MLEM reconstruction with muon statistics corresponding to 1 h exposure, full detector coverage. The true momentum of each muon was used in the reconstructions.

Table 1. Inspection time for 0% missing and 0% of false alarm for different volumes.

source volume (l)	15	10	5	2
average inspection time (min)	<1.0	2	4	6

— the modelling of the dimensions and positions of the muon detectors as sensitive media able to recognize the crossing of ionizing particles, recording hit coordinate and kinematic quantities; and
— all the physical processes for the interactions of muons and secondary particles in the transport through different volumes and materials: the energy loss by ionization, the delta-electron emission, multiple scattering, Bremsstrahlung radiation, nuclear interactions and muon decay.

(a) Realistic detector

Simulated data are reconstructed with the MLEM algorithm. The tomographic image shown in figure 6*b* is obtained with 1 h data and assuming perfect knowledge of each muon's momentum. The image is outstanding if compared with the model image in figure 6*a*, obtained with GEANT4 information of the linear scattering density of the simulated geometry materials.

As shown in figure 6, the detectors have complete coverage of the BF (the detectors are approx. 40 m in vertical length). Such a set-up would be impossible in terms of total cost, weight and its unwieldy nature. Practically speaking, only a small portion of the furnace would be imaged at any one time, by using two or more detectors of some reduced size. We propose to place two detectors of $5 \times 5\,\mathrm{m}^2$ surface area (both at the same vertical position) around the BF. With this horizontal set-up, sketched on the left of figure 7, the best images can be produced since muons travelling in both directions are collected, and the track density in voxels is symmetric even if closer in proximity to the furnace axis. Moreover, the horizontal set-up selects muons which have crossed a shorter length of the BF material, resulting in smaller momentum loss. The height of the detectors

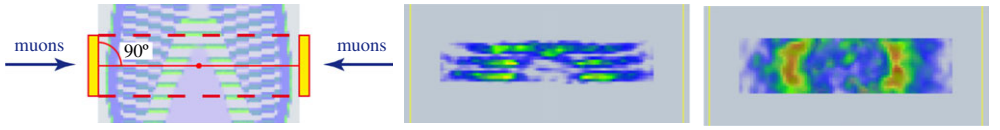

Figure 7. A sketch of the realistic detector set-up is shown on the left. On the right, reconstructed images obtained with a horizontal realistic detector of 5 × 5 m^2 and muon statistics corresponding to 15 h of data-taking. The true momentum of each muon was used in the reconstructions. The side view image slice is shown in the centre, the horizontal view on the right.

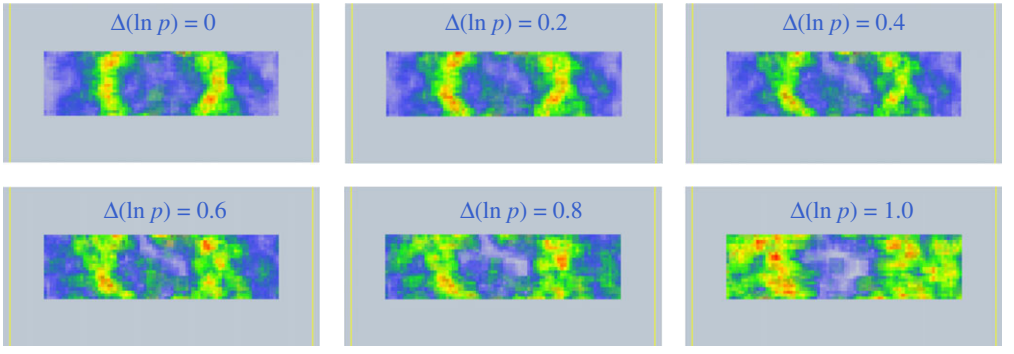

Figure 8. BF images reconstructed using the real detector set-up as described in the text. The muon momentum used in the MLEM algorithm is set to the true momentum smeared with a Gaussian-distributed random term. From top-left to bottom-right, the momentum has an error ranging from 0 ($\Delta \ln(p) = 0$) to 50% ($\Delta \ln(p) = 1$).

is arranged to preferentially image the region with higher density rings, which corresponds to the cohesive zone and the structure of the layers of coke and ore as shown in figure 7.

Reconstructed images obtained with a model of a realistic detector using the MLEM algorithm (assuming true muon momentum) are shown in figure 7. The images are projected on the side view plane (centre) and on the horizontal view plane (right). The central part of the BF is correctly reconstructed: the higher density ring of the cohesive zone is clearly visible and the dead man zone is reconstructed with a very low average density. However, using fixed muon momentum results in a very poor image reconstruction.

(b) Momentum measurement

As described in §3c, an estimate of the muon momentum is crucial for good MLEM algorithm results. To quantify the required muon momentum precision, we perform several BF image reconstructions using the true momentum smeared with a random Gaussian-distributed term to simulate the measurement error. The images in figure 8 are obtained with six different momentum spreads. The images show that a precision up to 50% of the momentum value ($\Delta \ln(p) = 1$) is sufficient to produce clear images of the furnace interior structure.

It is found that the muon detectors will be required to measure the muon momentum with a minimum precision of 50%, in addition to measuring the muon position and direction. We propose to use the basic equation of the multiple coulomb scattering to infer the muon momentum from a measurement of the variance of the scattering angle $\sigma^2_{\Delta\phi}$ when X/X_0 is known as

$$p \sim \sqrt{\frac{X}{X_0}\frac{1}{\sigma^2_{\Delta\phi}}}. \tag{4.1}$$

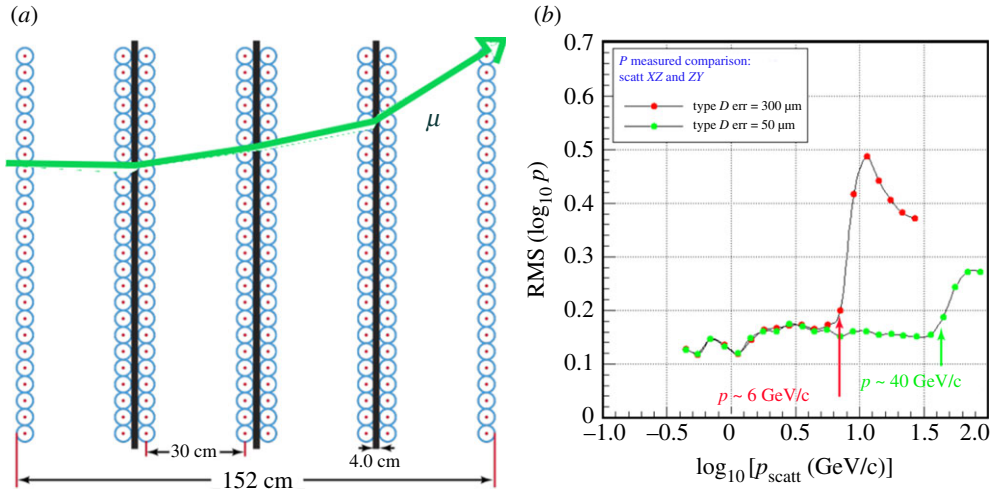

Figure 9. Detector design. (*a*) Scheme of a detector capable of measuring the muon momentum through quantification of the scattering in iron plates. Layers of drift tubes are shown in blue, iron plates in black. An example of muon trajectory is drawn in green with (illustratively) exaggerated scattering. (*b*) Measured momentum resolution for two values of the detector resolution: 300 μm and 50 μm. In the latter case, the momentum is well predicted up to $p = 40$ GeV/c.

Our detector design foresees the measurement of the muon position in sensitive planes of drift tubes, and the measurement of the muon momentum through the proper quantification of the muon scattering in iron plates of constant and known thickness inserted in between. A sketch of the detector is shown in figure 9*a*. It is built with six layers of drift tubes of radii 2.5 cm. Three iron plates of thickness 4 cm are interposed. Drift tubes measure the distance of the muon track from the tube axis with very good precision, typically 300 μm and down to 50 μm. The longitudinal coordinate along the tube axis is measured with a poorer precision of the order of 10 cm. In order to infer the momentum measurement precision for this detector set-up, we compare the momentum value obtained from scattering information with the true momentum value available from the simulation. The procedure is described as follows. For each muon, a combination of the values of the scatterings in the iron plates of the two detectors is computed and the scattering momentum is obtained from equation (4.1). The scattering momentum distribution of the muon collection is divided into intervals. For each interval, the scattering momentum average (p_{scatt}) and the true momentum average (p) are compared. The RMS of the logarithm distribution of the true momentum versus the logarithmic of p_{scatt} is shown in figure 9*b*. The graph shows that for a detector precision of 300 μm the momentum is measured with good resolution up to 6 GeV/c, and for a precision of 50 μm the momentum is measured with good resolution up to 40 GeV/c. Higher muon momentum manifest scatterings that are smaller than the measurement error, and thus are not measurable.

Images are reconstructed with the MLEM algorithm, and for each muon the p-value of the corresponding p_{scatt} interval is assigned. Figure 10 compares the projection of the images on the horizontal plane, reconstructed using the true momentum (*a*) and the measured momentum of a detector of 50 μm resolution (*b*). A dataset corresponding to 4 h in the first row, and 2 h in the second row, is used. The images obtained with measured momentum show a very good quality contrast of the cohesive zone ring and ore-coke layers, even if few hours of data-taking are considered.

(c) Burden drop

In a time scale of approximately 8 h, the loaded material from the top of the furnace reaches the furnace base. Therefore, it is clearly unrealistic to use a furnace image reconstructed with several

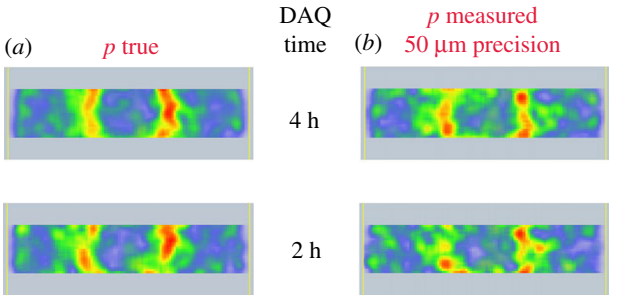

Figure 10. MLEM reconstructed images using measured momentum with the detector of 50 µm precision described in the text. True momentum images on the left (*a*) are compared with muon measured images on the right (*b*). A dataset corresponding to 4 and 2 h of data-taking is used. A projection of the images on the horizontal plane is visualized. The cohesive zone ring and of the ore-coke layers are clearly visible.

hours of muon data using a static furnace geometry (i.e. where the ore and coke layers do not descend with time).

In order to obtain realistic results, we simulate the 'burden drop' using a mixture of muon datasets. For each dataset, the muons interact with a different furnace model having the layers shifted downward by 25 cm. The tomographic reconstruction images of the mixed sample do not show any structure even using the true momentum (figure 11, first row), unless the information regarding the descent velocity of the material is considered. Indeed, satisfying images are reconstructed when the muon impact point on the furnace is shifted upwards by the same amount corresponding to the material drop, as can be seen in the second row of figure 11. In real life, if the velocity is not precisely known, several images can be produced using different velocity values. The sharpest image will show the internal BF structures, and will also give a measurement of the descent velocity. This method appears quite robust against velocity value precision, as can be seen in the last row of figure 11, where the BF structures are still visible in both projections even with a 50% error on the velocity value.

5. Canister spent fuel bar detection

The inspection and verification of heavy shielded spent nuclear fuel (SNF) containers in case of loss of continuity of knowledge is a challenging task, which is becoming of increasing interest for the storage facilities around the world. The minimal requirement for potential verification techniques is the detection of the absence of significant quantities of nuclear material (such as fuel bars). In this vein, muon tomography techniques are emerging as a promising candidate [23–26,35].

Here, we develop an absorption-based algorithm, which is novel and gives promising results for the detection of missing SNF bars in storage canisters. A brief description of the algorithm is given in §5b and the corresponding results are presented in the following sections. Preliminary results only are presented hereafter since a dedicated analysis is still ongoing.

(a) Canister Model

A complete and accurate CASTOR@21 Cask is modelled in GEANT4 framework geometry. The model specifications consider an iron-made cast with a height of 4.88 m and diameter of approximately 2.4 m. The inner cavity dimensions are: length 4.15 m, diameter 1.53 m. The canister hosts 24 slots of stainless steel lids for permanent storage of SNF bundles placed in tight spaces. The muon detectors implemented in the simulation consist of eight layers of vertical cylindrical drift tubes each of 2.5 cm radius and 6 m height, surrounding the canister

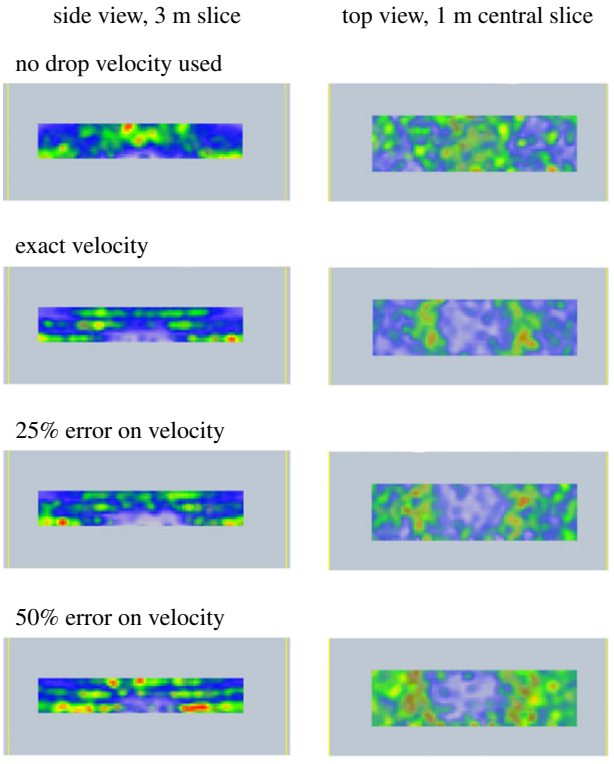

Figure 11. Reconstructed images of a mixture of datasets obtained from the simulation of four furnace models. In each model, the layers are shifted downward according to the burden drop velocity. The side and horizontal view of the reconstruction are shown. From top to bottom: in the first row no drop information is considered; in the second row the exact velocity information is used in the reconstruction; and in the third and fourth rows the velocity uncertainties of 25% and of 50% are added, respectively. The true momentum of each muon was used in the reconstructions.

for full coverage. Figure 12*a* shows the cross section of the canister design, and figure 12*b* shows the cross section of the canister and the surrounding detectors as implemented in the GEANT4 simulation. The cosmic muon flux is implemented in the simulation, and all required physics processes for the transport and interaction of the particles throughout the canister (multiple Coulomb scattering, ionization, Bremsstrahlung, pair production, etc.). We simulate data using a canister with complete fuel loading, and with one or two missing fuel bar(s). Datasets, both with no experimental error and with Gaussian errors due to detector precision, are generated. For each set-up, we generate 60 million muons (corresponding to 12 h of data-taking).

Two imaging techniques are used to present preliminary images of the CASTOR@21 container: the muon transmission and the MLEM algorithm. In the first case, the number of muons entering and exiting the castor is recorded in each voxel along the muon path (transmitted muon density). The final image is obtained as the difference between the complete castor transmitted muon density and the castor with a missing bar density, as in figure 13*a*. Although the image shows the location of the missing bar, it is not trivial to infer a meaningful physical quantity correlated with image density scale. In figure 13*b*, the image obtained with the MLEM algorithm is shown. In this case, one day of data-taking and perfect knowledge of the muon momentum are necessary to obtain a clear image, and the image density scale is correlated with the product of the density and the average Z of the materials. As the transmitted muon density image gives promising results, we pursued the development of a completely novel algorithm (as described in §5b) based on

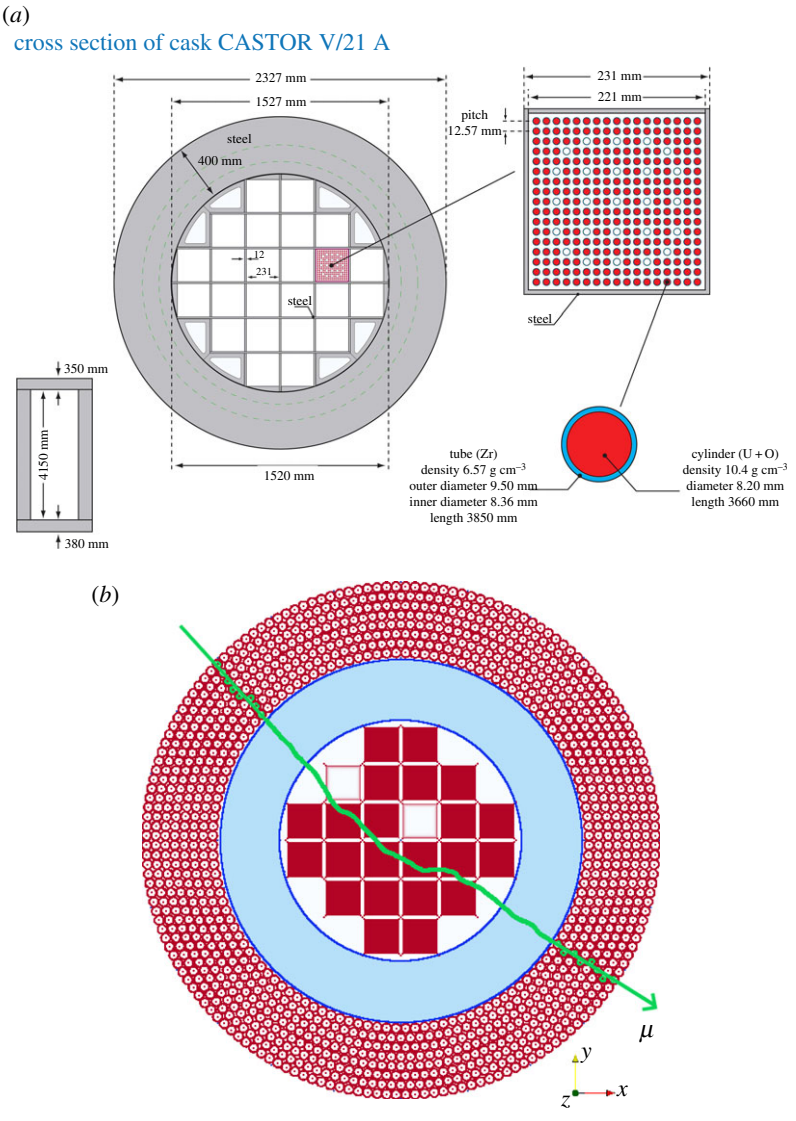

Figure 12. Cross section of the canister design: (*a*) the horizontal view of the canister is sketched, together with an enlarged slot for the fuel bundle and an enlarged pin; (*b*) a screen-shot of the geometry implemented in the GEANT4 simulation. The cross section of the canister with two missing bars and the surrounding detectors are shown. An example of a muon track crossing the canister is superimposed on the geometry volumes.

the stopped and transmitted muons information, and capable of yielding meaningful physical information regarding the material distribution.

(b) μCT algorithm

Our innovative μCT algorithm analyses the information regarding the fraction of absorbed muons along a so-called Line-of-Response (LoR, often used in PET tomography), and compares this information with the theoretical absorption ratio derived from the muon energy distribution and the traversed material thickness. A functional is constructed with the sum of the squared discrepancies between the experimental and predicted number of absorbed muons in each LoR. The outcome of the minimization of the functional gives the material average stopping power in

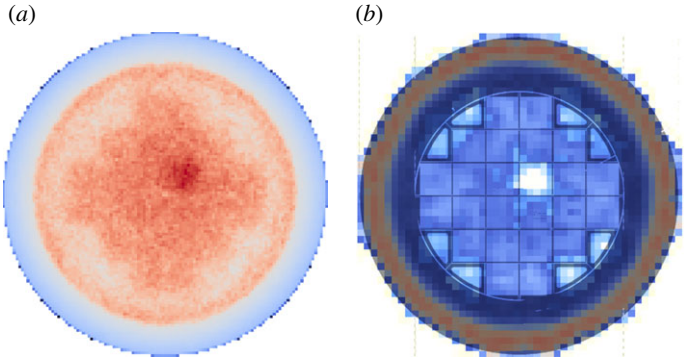

Figure 13. Cross section of the canister image reconstruction, obtained as an average of horizontal slices. The simulated data have one missing fuel bar. (*a*) Image obtained with the track density in voxels, subtracting a canister with missing bar from the complete canister image; 3 h of data, voxel dimensions: $2 \times 2 \times 5\ \mathrm{cm}^3$. (*b*) The MLEM reconstruction with real momentum. Voxel dimensions: $5 \times 5 \times 10\ \mathrm{cm}^3$, data-taking one day. The $\alpha\beta$-trim filter is applied to the image. The sketch of the CASTOR section is superimposed on the reconstructed image on the right to show the expected position of the missing fuel bar.

each voxel of the imaging volume (in $\mathrm{GeV\,cm}^{-1}$), which is related to the density of the material:

$$\left\langle \frac{\mathrm{d}E}{\mathrm{d}x} \right\rangle_{\mathrm{voxel}} \sim \frac{Z}{A}\rho. \tag{5.1}$$

The details of the algorithm are given as follows. The volume to be reconstructed is divided into a collection of voxels, and each voxel is initialized with a zero value of the stopping power: $\langle \mathrm{d}E/\mathrm{d}x \rangle_{\mathrm{voxel}} = \epsilon_0$. As regards LoR definition: the cylindrical lateral surface of the canister is ideally divided into pixels. Every pair of pixels makes up an LoR, i.e. $\mathrm{LoR} = (\mathrm{pixel}_{\mathrm{IN}}, \mathrm{pixel}_{\mathrm{OUT}})$.

Each muon of the collection is assigned to an LoR if it enters $\mathrm{pixel}_{\mathrm{IN}}$ and it exits from $\mathrm{pixel}_{\mathrm{OUT}}$. If the muon is absorbed while crossing the castor, the projection from the in-going direction to the canister lateral surface is computed and the $\mathrm{pixel}_{\mathrm{OUT}}$ intersected by the projection is considered. No scattering information is employed in this algorithm, except for rejecting the events whose exit point is too far from the in-going direction projection.

For each LoR^i, the following data are recorded: the number of total muons entering $\mathrm{N}^i_{\mathrm{in}}$, the number of absorbed muons $\mathrm{N}^i_{\mathrm{stop}}$. The LoR ray-tracing is performed from the middle position of $\mathrm{pixel}_{\mathrm{IN}}$ to the middle position in $\mathrm{pixel}_{\mathrm{OUT}}$ along a straight path and the set of the crossed path in each voxel x^i_j (where $i =$ LoR index, $j =$ voxel index) is allocated for the LoR.

After this initialization step, the algorithm procedure is iterative. At each iteration k, the following calculations are carried out:

— $E^i = \sum_j x^i_j \cdot \epsilon_j$: energy loss in each LoR^i;
— $\mathrm{Prob}(E^i) = \int_0^{E^i} (\mathrm{d}N/\mathrm{d}E)(\theta)\,\mathrm{d}E$: probability of a muon to have an energy below E^i, where $\mathrm{d}N/\mathrm{d}E(\theta)$ is the cosmic muon spectra distribution with a zenith angle dependency;
— $N^i_{\text{stop-predict}} = N^i_{\mathrm{in}} * \mathrm{Prob}(E^i)$: number of expected absorbed muons in each LoR;
— $F(\{\epsilon_j\}) = \sum_i (N^i_{\text{stop-predict}} - N^i_{\mathrm{stop}})^2/\sigma^2$: functional to be minimized, where σ^2 is the variance;
— evaluation of the gradient $\Delta F(\epsilon_j)$ of F;
— steepest descent minimization; and
— voxel stopping power update: $\epsilon_j^{(k+1)} = \epsilon_j^{(k)} - \mathrm{step} * \nabla F(\{\epsilon_j^{(k)}\})$, where the value for the scalar step is derived from a one-dimensional minimization.

The algorithm performs well and only a few iterations, approximately 10, are needed to reach the convergence. Results are presented in the next section.

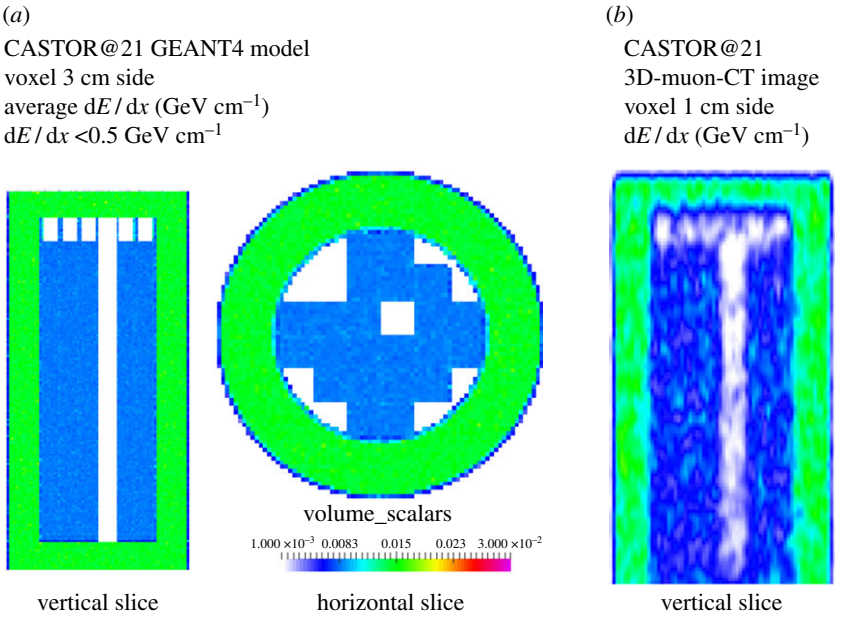

Figure 14. Canister images of the stopping power of the materials. (*a*) The model image obtained computing for each voxel the average of the energy deposit of the muons crossing the voxel, from the GEANT4 tracking routines information. The vertical and horizontal image slices are shown. (*b*) μCT image reconstruction using 12 h of data. The vertical slice is shown, where the missing bar is perfectly spotted.

(c) Results

The images are reconstructed with the μCT algorithm using 1–12 h of cosmic muons data-taking, and they are smoothed with an anisotropic Gaussian filter in order to exploit the extended degree of translational invariance of the canister along the vertical direction. The results are rather good: it is possible to obtain acceptably clear three-dimensional images of the stopping power of the inspected material using 12 h of data, as shown in figure 14*b*. Moreover, the stopping scale values of the reconstructed images are in good agreement with the model shown in figure 14*a*. The GEANT4 model image is obtained by computing for each voxel the average of the energy loss of the muons crossing it; these values are available via the GEANT4 tracking routines.

Figure 15 shows the time evolution of the reconstructed images: the cross-section image obtained with an average over the horizontal slices in the vertical range including the fuel bars is shown. In figure 15*a*, data used in the reconstruction corresponds to 1 h of time. In figure 15*b*, 12 h of data are processed. Although the image in (*b*) is better defined, the missing bars can also be clearly identified in image (*a*).

A realistic detector response is simulated as well. The detector modelled in the simulation is assembled with eight layers of drift tubes each of 2.5 cm radius placed vertically, for a full canister coverage, as shown in the sketch of figure 12. The front-end electronics for detector readout are placed at both tube ends for a twofold reading of the tube signals to allow vertical coordinate measurement. In the horizontal plane, the track position and trajectory are measured from its straight-line fit. The vertical coordinate is measured from the difference of the two tube ends' signals reading. The position resolution is approximately 300 μm in the horizontal plane and approximately 20 cm in the vertical coordinate. The reconstructed images with and without experimental error are shown in figure 16 for 12 h of data-taking. The cross-sectional image obtained with an average over the horizontal slices using simulated data with the described experimental error are very clear, and the missing bars can be clearly identified.

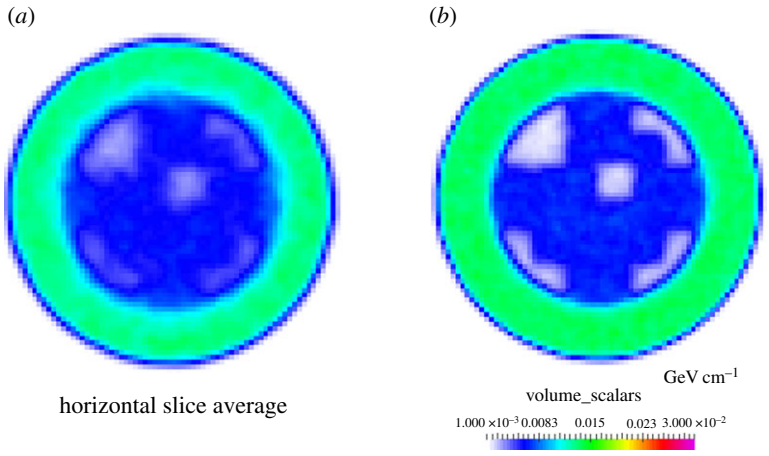

Figure 15. Reconstructed image with the μCT algorithm. The cross-sectional image obtained with an average of horizontal slices is shown for different acquisition times: (*a*) 1 h data and (*b*) 12 h.

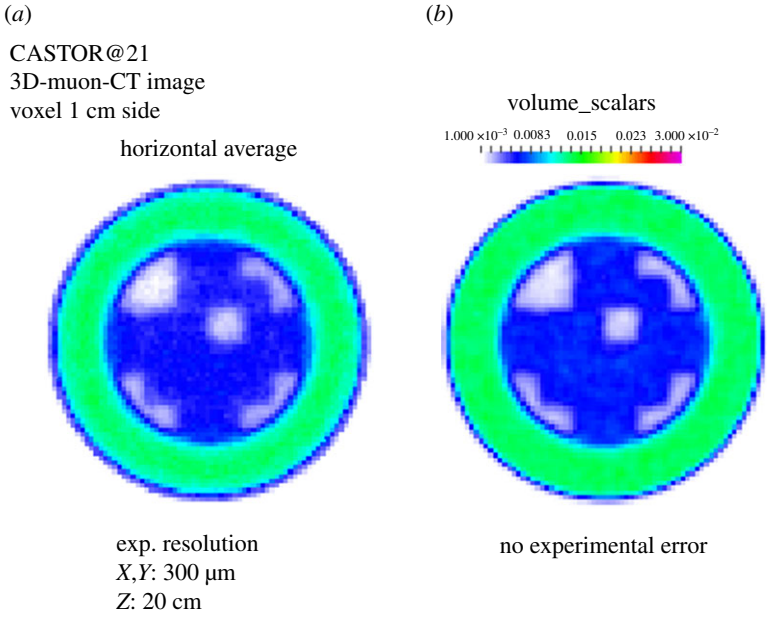

Figure 16. Reconstructed image with the μCT algorithm using 12 h of simulated data of a realistic detector with position resolution of 300 μm in the horizontal plane and of 20 cm in the vertical plane. The average of horizontal slices is shown, both with experimental error in (*a*), and with perfect position knowledge in (*b*).

6. Conclusion

The successful results of muon tomography techniques applied to different types of simulated applications are presented in this paper. An appropriate algorithm is applied for each application. Our results show that a muon tomography scanner for cargo containers loaded with scrap metal fully meets the requirements of the steel industry. As shown using the MLEM algorithm with muon momentum estimation, it is possible to detect in approximately 4 min a 5 l shielded radioactive source, with 100% efficiency and less than 1% of FA. The required time increases up to 6 min for a 2 l source.

Applied to imaging of a blast furnace, muon tomography is shown to give meaningful images by using a realistic detector $5 \times 4\,m^2$ wide (including iron plates for muon momentum measurements) of the cohesive high-density zone and of the ore-coke layers in 2–4 h of data-taking. The images are obtained with the MLEM algorithm using the muon momentum measured by the detectors, and data are simulated considering the detector experimental error and the dynamic evolution of the furnace burden drop. This is valuable information in order to optimize the furnace process and decrease the fuel burning.

The canister inspection for the detection of missing SNF bars is used to probe our novel algorithm μCT based on muon tomography absorption. The results are excellent: a few hours of simulated data of cosmic muons crossing a CASTOR@21 canister detected by a realistic detector with experimental resolution are sufficient to spot the missing fuel bars.

Data accessibility. Code available on github: https://github.com/OpenCMT/.

Competing interests. The authors declare that they have no competing interests.

Funding. The research being reported in this publication was supported by grants from the European Union Research Fund for Coal and Steel: grant no. RFSR-CT-2010-00033 for the MU-STEEL project *Muon scanner to detect radioactive sources hidden in scrap metal containers*, and grant no. RFSR-CT-2014-00027 for MU-BLAST project *Study of the capability of muon tomography to map the material composition inside a blast furnace*. In addition, the authors of this publication have benefitted from research support from Istituto Nazionale di Fisica Nucleare sezione di Padova and Legnaro Laboratories.

Acknowledgements. Our deep appreciation goes to Franco Gonella and all the technicians in the INFN Legnaro Laboratory for making available and working the Muon Tomography Station. The simulation validation was carried out by means of comparison with real data reconstructions.

References

1. Checchia P. 2016 Review of possible applications of cosmic muon tomography. *J. Instrum.* **11**, C12072. (doi:10.1088/1748-0221/11/12/C12072)
2. Borozdin KN, Hogan GE, Morris C, Priedhorsky WC, Saunders A, Schultz LJ, Teasdale ME. 2003 Surveillance: radiographic imaging with cosmic-ray muons. *Nature* **422**, 277. (doi:10.1038/422277a)
3. Priedhorsky WC, Borozdin KN, Hogan GE, Morris C, Saunders A, Schultz LJ, Teasdale ME. 2003 Detection of high-Z objects using multiple scattering of cosmic ray muons. *Rev. Sci. Instrum.* **74**, 4294–4297. (doi:10.1063/1.1606536)
4. MU-BLAST. 2014 Study of the capability of muon tomography to map the material composition inside a blast furnace. EU publications Research found for coal and steel RFSR-CT-2014-00027.
5. Xianfeng H *et al.* 2018 Exploring the capability of muon scattering tomography for imaging the components in the blast furnace. *ISIJ Int.* **58**, 35–42. (doi:10.2355/isijinternational.ISIJINT-2017-384)
6. Aström E *et al.* 2016 Precision measurements of linear scattering density using muon tomography. *J. Instrum.* **11**, P07010. (doi:10.1088/1748-0221/11/07/p07010)
7. Shinotake A, Matsuzaki S, Kunitomo K, Naito M, Hashimoto M, Hatanaka A, Nagane T, Nagamine K, Tanaka H. 2009 Probing the inner structure of blast furnaces by cosmic-ray muon radiography. *Proc. Jpn Acad Ser B Phys Biol. Sci.* **81**, 257–260. (doi:10.2183/pjab.81.257)
8. Gilboy NNWB, Jenneson PM. 2005 Industrial thickness gauging with cosmic-ray muons. *Radiat. Phys. Chem.* **74**, 454–458. (doi:10.1016/j.radphyschem.2005.08.007)
9. Sauerwald J, Franzen A, Fischer A, Buhles T, Janz J. Investigation of the coke network and cohesive zone by muon tomography. *Stahl und Eisen* **134**, 29–40.
10. George E. 1955 Cosmic rays measure overburden of tunnel. *Commonwealth Engineer* **1955**, 455–457.
11. Alvarez LW *et al.* 1970 Search for hidden chambers in the pyramids. *Science* **167**, 832–839. (doi:10.1126/science.167.3919.832)
12. Morishima K *et al.* 2017 Discovery of a big void in Khufu's Pyramid by observation of cosmic-ray muons. *Nature* **552**, 386–390. (doi:10.1038/nature24647)
13. Jourde K, Gibert D, Marteau J, De Bremond D'ars J, Gardien S, Girerd C, Ianigro J-C, Carbone D. 2013 Effects of upward-going cosmic muons on density radiography of volcanoes. (http://arxiv.org/abs/1307.6758).

14. Marteau J, Gibert D, Lesparre N, Nicollin F, Noli P, Giacoppo F. 2012 Muons tomography applied to geosciences and volcanology. *Nucl. Instrum. Methods Phys. Res. A* **695**, 23–28. (doi:10.1016/j.nima.2011.11.061)
15. Anastasio A *et al.* 2013 The MU-RAY detector for muon radiography of volcanoes. *Nucl. Instrum. Methods Phys. Res. A* **732**, 423–426. (doi:10.1016/j.nima.2013.05.159)
16. Carbone D, Gibert D, Marteau J, Diament M, Zuccarello L, Galichet E. 2014 An experiment of muon radiography at Mt. Etna (Italy). *Geophys. J. Int.* **196**, 633–643. (doi:10.1093/gji/ggt403)
17. Nagamine K, Iwasaki M, Shimomura K, Ishida K. 1995 Method of probing inner-structure of geophysical substance with the horizontal cosmic-ray muons and possible application to volcanic eruption prediction. *Nucl. Instrum. Methods Phys. Res. A* **356**, 585–595. (doi:10.1016/0168-9002(94)01169-9)
18. Malmqvist L, Jnsson G, Kristiansson K, Jacobsson L . 1979 Theoretical studies of in-situ rock density determinations using underground cosmic-ray muon intensity measurements with application in mining geophysics. *GEOPHYSICS* **44**, 1549–1569. (doi:10.1190/1.1441026)
19. Gómez H, Carloganu C, Gibert D, Jacquemier J, Karyotakis Y, Marteau J, Niess V, Katsanevas S, Tonazzo A. 2016 Studies on muon tomography for archaeological internal structures scanning. *J. Phys: Conf. Ser.* **718**, 052016. (doi:10.1088/1742-6596/718/5/052016)
20. Saracino G *et al.* 2017 Imaging of underground cavities with cosmic-ray muons from observations at Mt. Echia (Naples). *Sci. Rep.* **7**, 1181. (doi:10.1038/s41598-017-01277-3)
21. Dedenko LG *et al.* 2014 Prospects of the study of geological structures by muon radiography based on emulsion track detectors. *Bull. Lebedev Phys. Inst.* **41**, 235–241. (doi:10.3103/S1068335614080065)
22. Klinger J *et al.* 2015 Simulation of muon radiography for monitoring CO 2 stored in a geological reservoir. *Int. J. Greenhouse Gas Control* **42**, 644–654. (doi:10.1016/j.ijggc.2015.09.010)
23. Jonkmans G, Anghel VNP, Jewett C, Thompson M. 2013 Nuclear waste imaging and spent fuel verification by muon tomography. *Ann. Nucl. Eng.* **53**, 267–273. (doi:10.1016/j.anucene.2012.09.011)
24. Clarkson A *et al.* 2015 Characterising encapsulated nuclear waste using cosmic-ray Muon Tomography (MT). In *4th International Conference on Advancements in Nuclear Instrumentation Measurement Methods and their Applications (ANIMMA) 2015, Lisbon, Portugal, 20–24 April*. New York, USA: IEEE. (doi:10.1109/ANIMMA.2015.7465529)
25. Poulson D, Durham JM, Guardincerri E, Morris CL, Bacon JD, Plaud-Ramos K, Morley D, Hecht AA. 2017 Cosmic ray muon computed tomography of spent nuclear fuel in dry storage casks. *Nucl. Instrum. Methods Phys. Res. A* **842**, 48–53. (doi:10.1016/j.nima.2016.10.040)
26. Chatzidakis S, Choi CK, Tsoukalas LH. 2016 Analysis of spent nuclear fuel imaging using multiple Coulomb scattering of cosmic Muons. *IEEE Trans. Nucl. Sci.* **63**, 2866–2874. (doi:10.1109/TNS.2016.2618009)
27. Borozdin K, Greene S, Lukić Z, Milner E, Miyadera H, Morris C, Perry J. 2012 Cosmic ray radiography of the damaged cores of the Fukushima reactors. *Phys. Rev. Lett.* **109**, 152501. (doi:10.1103/PhysRevLett.109.152501)
28. Perry J *et al.* 2013 Imaging a nuclear reactor using cosmic ray muons. *J. Appl. Phys.* **113**, 184909. (doi:10.1063/1.4804660)
29. Olive KA. 2014 Review of particle physics. *Chin. Phys.* **C38**, 090001. (doi:10.1088/1674-1137/38/9/090001)
30. Schultz LJ, Blanpied GS, Borozdin KN, Fraser AM, Hengartner NW, Klimenko AV, Morris CL, Oram C, Sossong MJ. 2007 Statistical reconstruction for cosmic ray Muon tomography. *IEEE Trans. Image Process.* **16**, 1985–1993. (doi:10.1109/TIP.2007.901239)
31. Benettoni M *et al.* 2013 Noise reduction in muon tomography for detecting high density objects. *J. Instrum.* **8**, P12007. (doi:10.1088/1748-0221/8/12/p12007)
32. Agostinelli S *et al.* 2003 Geant4-a simulation toolkit. *Nucl. Instrum. Methods Phys. Res. A* **506**, 250–303. (doi:10.1016/S0168-9002(03)01368-8)
33. Bonechi L. 2005 Development of the ADAMO detector: test with cosmic rays at different zenith angles. In *Proc. of the 29th Int. Cosmic Ray Conf. 2005, Pune, India, 3–10 August*. Mumbai, India: Tata Institute of Fundamental Research.
34. Bednar J, Watt T. 1984 Alpha-trimmed means and their relationship to median filters. *IEEE Trans. Acoust. Speech Signal Process.* **32**, 145–153.
35. Checchia P *et al.* 2017 Muon Tomography for spent nuclear fuel control. *ESARDA Bull.* **54**, 2–5.